TITLE: Seismic reflection imaging of the low-angle Panamint normal fault system, eastern California

AUTHORS (FIRST NAME, LAST NAME): Ryan D. Gold[1], William J. Stephenson[1], Richard W. Briggs[1], Christopher B. DuRoss[1], Eric Kirby[2], Edward Woolery[3], Jaime Delano[1], Jack K. Odum[1]

INSTITUTIONS:
[1]U.S. Geological Survey, Geologic Hazards Science Center, Golden, CO 80401, U.S.A.
[2]College of Earth, Ocean, and Atmospheric Sciences, Oregon State University, Corvallis, OR 97331, U.S.A.
[3]Earth and Environmental Sciences, University of Kentucky, Lexington, KY 40506, U.S.A.

KEY POINTS:

- Seismic reflection imaging used to explore crosscutting relationships between low- and high-angle faults, Panamint Valley, CA
- A low-angle normal fault appears faulted and rotated by higher-angle structures associated with Panamint Valley fault zone
- Results interpreted to indicate that at shallow depths, the low-angle normal fault is probably no longer active

This is the author manuscript accepted for publication and has undergone full peer review but has not been through the copyediting, typesetting, pagination and proofreading process, which may lead to differences between this version and the Version of Record. Please cite this article as doi: 10.1029/2020JB020243

Abstract

Shallowly dipping (<30º) low-angle normal faults (LANFs) have been documented globally; however, examples of active LANFs in continental settings are limited. The western margin of the Panamint Range in eastern California is defined by a LANF that dips west beneath Panamint Valley and has evidence of Quaternary motion. In addition, high-angle dextral-oblique normal faults displace middle to late Quaternary alluvial fans near the range front. To image shallow (<1 km depth), crosscutting relationships between the low- and high-angle faults along the range front, we acquired two high-resolution P-wave seismic reflection profiles. The northern, 4.6-km-long profile crosses the 2-km-wide Wildrose graben and the southern, 0.8-km-long profile extends onto the Panamint Valley playa, ~7.5 km S of Ballarat, CA. The profile across the Wildrose graben reveals a robust, low-angle reflector interpreted to represent the LANF separating Plio-Pleistocene alluvial fanglomerate and Proterozoic meta-sedimentary deposits. High-angle faults interpreted in the seismic profile correspond to fault scarps on Quaternary alluvial fan surfaces. Interpretation of the reflection data suggests that the high-angle faults vertically displace the LANF up to 80 m within the Wildrose graben. Similarly, the profile south of Ballarat reveals a low-angle reflector, which appears both rotated and displaced up to 260 m by high-angle faults. These results suggest that near the Panamint range front, the high-angle faults are the dominant active structures. We conclude that, at least at shallow (<1 km) depths, the LANF we imaged is not active today.

1. Introduction

Slip along <30º-dipping low-angle normal faults (LANFs) is not mechanically favorable under typical frictional conditions [0.6—0.85, *Byerlee*, 1978; *Sibson*, 1994]; rather, traditional mechanical theory predicts that normal faulting should occur along >45º-dipping faults [*Anderson*, 1951]. This theory is supported by the observation that the majority of instrumented normal faulting earthquakes occur along focal planes dipping between 30-60º at nucleation depths ranging from 6-15 km [*Collettini*, 2011; *Jackson*, 1987; *Wernicke*, 1995], which is inconsistent with seismogenic motion along shallowly dipping fault planes. Despite the lack of mechanically favorable conditions and the dearth of seismologic observations consistent with motion along shallowly dipping normal fault planes, LANFs have been documented globally in a wide range of settings, including the Basin and Range Province in the western U.S., the Canadian Cordillera, the Apennines in Italy, the Alps, the Aegean, Turkey, Tibet, Thailand, Papua New Guinea, and mid-ocean ridges [*Webber et al.*, 2018 and references therein]. A number of studies have explored this "paradox" [*Wernicke*, 1995], with some emphasizing the role that "domino-style" or rolling-hinge mechanisms may play in rotating steeply dipping (>45º) faults into shallow and presumably nonseismogenic orientations [*Mizera et al.*, 2019; *Proffett*, 1977]. However, unambiguous examples of fault initiation and continued slip on shallowly inclined planes are numerous [e.g., *Morley*, 2009; *Wernicke*, 1995].

A growing body of literature focused on re-located seismicity [*Chiaraluce et al.*, 2007], geodetic observations [*Hreinsdóttir and Bennett*, 2009], fault gouge and friction [*Haines et al.*, 2014; *Haines and van der Pluijm*, 2012], and numerical modeling [*Lecomte et al.*, 2012; *Vadacca et al.*, 2016] suggests that the effective friction on LANFs is sufficiently low (<0.3) to facilitate slip along shallowly dipping faults. Numerical models suggest that slip along LANFs

occurs in a slip-hardening regime, which may inhibit large earthquakes [*Lecomte et al.*, 2012]. This framework is consistent with the lack of observed focal mechanisms observed for shallowly dipping normal faults [*Collettini*, 2011].

In a global inventory of 49 active LANFs in continental crust with slip-rate constraints Webber et al. [2018] show that only six of those faults are confirmed to be unambiguously active. Of these active faults, the Mai'iu fault in Papua New Guinea [*Mizera et al.*, 2019] is among the fastest slipping known active LANFs, with a dip-slip rate of 11.7 ± 3.5 mm/yr since 5.5 ka [*Webber et al.*, 2018]. Other active LANFs have been documented using a range of techniques including (1) geodetic observations of aseismic creep on the Alto Tiberina LANF in Italy [*Bennett and Hreinsdóttir*, 2009], (2) geophysical [*Abbott et al.*, 2001] and geologic [*Caskey et al.*, 1996] observations that suggest slip on a <30º dipping, ~10-km-long section of the Dixie Valley fault when it ruptured in 1954, (3) geologic and structural observations focused on the Traverse Mountains that indicate a 5-7 km-long section of the Wasatch fault dips ~35 degrees [*Bruhn et al.*, 1992], and (4) seismic observations supporting a 20–30º dip for part of the Wasatch fault zone near Salt Lake City [*Pang et al.*, 2020].

In this investigation, we seek to evaluate whether a LANF bounding the western margin of the Panamint Range in eastern California is active or if it is crosscut by the high-angle dextral-oblique Panamint Valley fault zone (Fig. 1). We use high-resolution seismic reflection imaging to resolve the crosscutting relationships between these two styles of faults. Results from this work suggest that the LANF imaged at two locations appears cut by the more steeply dipping Panamint Valley fault zone, suggesting high-angle faulting is now the dominant style of active faulting in this location.

2. Geologic Framework of Panamint Valley

Panamint Valley is an extensional basin situated east of the Sierra Nevada and west of Death Valley. Panamint Valley lies within the southern Walker Lane and Eastern California shear zone, where modern deformation is characterized by dextral shear accommodated along three major faults systems: the Death Valley-Fish Lake Valley, Panamint Valley, and Owens Valley fault systems (Fig. 2) [*Stewart*, 1988; *Wesnousky*, 2005]. East-west directed Basin and Range extension is also accommodated in this region. Panamint Valley and the surrounding mountains are composed of these primary geologic units: Proterozoic crystalline and metasedimentary rocks in the Panamint Range [*Albee*, 1981; *Labotka et al.*, 1980]; Tertiary Nova Basin deposits, which are interpreted to be the depositional record of exhumation associated with the Panamint Range [*Hodges et al.*, 1989]; Plio-Pleistocene alluvial fan deposits [*Jayko*, 2009] and Pleistocene pluvial lacustrine deposits [*Jayko et al.*, 2008; *Smith*, 1976].

LANFs in the western U.S. have their roots in deep-seated detachment faults (metamorphic core complexes) formed during mid-Tertiary extension of overthickened crust adjacent to the North American Cordillera [*Axen*, 2004; *Coney*, 1987; *Coney and Harms*, 1984; *Crittenden et al.*, 1980; *Wernicke*, 1995]. Panamint Valley is thought to have formed starting ca. 15 Ma, at which time exhumation occurred via slip on the west-dipping low-angle Emigrant detachment system [*Hodges et al.*, 1989]. The modern-day valley is younger than ~4 Ma [*Burchfiel et al.*, 1987], consistent with cessation and abandonment of the Emigrant detachment system at ~3-4 Ma [*Snyder and Hodges*, 2000]. The formerly continuous Emigrant detachment is cut by a combination of dextral and normal faults and subdivided into three segments, including the Emigrant, Panamint, and Slate Range detachments or LANFs [*Andrew and Walker*, 2009] (Fig. 2b). The LANF that delineates the western margin of the Panamint Range is exhumed and

visible in two key locations in Panamint Valley: the southern section of the Emigrant LANF near the Wildrose graben and the Panamint LANF (or Panamint detachment), between Happy and Redlands Canyons (Fig. 2b).

Steeply dipping dextral and normal faults formed within Panamint Valley in the Pliocene [*Andrew and Walker*, 2009; *Cichanski*, 2000; *Hopper*, 1947]. The distribution and geomorphic character of these high-angle faults (HAFs) along the western flank of the Panamint Range were first documented by Maxson [1950] and later characterized by Smith [1976]. These faults compose two primary fault systems: the dextral oblique Panamint Valley fault zone and the dextral Ash Hills fault (Fig. 2). The Panamint Valley fault zone slips dextrally at a rate of ~2.4 ± 0.8 mm/yr based on laterally offset Holocene alluvial fan features [*Zhang et al.*, 1990]. Preliminary rates of late Pleistocene vertical motion are proposed to locally reach ~3.3 mm/yr in regions where the fault steps right and exhibits a more north or northeast orientation [*Hofffman*, 2009]. The ratio of strike-slip to dip-slip motion appears to be largely a function of fault orientation. The Ash Hills fault has a dextral slip rate of 0.3-0.5 mm/yr, based on a laterally offset 4 Ma volcanic unit and offset 120-150 ka shorelines [*Densmore and Anderson*, 1997]. A paleoseismic trenching study along the southern Panamint Valley fault zone documented evidence for four surface-rupturing earthquakes since 4 ka [*McAuliffe et al.*, 2013], indicating Holocene activity on this fault. The Panamint Valley fault zone connects with the Hunter Mountain fault zone to the north, which slips dextrally at a rate of 3-4 mm/yr [*Oswald and Wesnousky*, 2002].

In this region, significant attention has focused on the geometry and recency of faulting along the LANF along the western margin of the Panamint Range. Burchfiel et al. [1987] document a faulted piercing line defined by the intersection of the subhorizontal base of a 3.7 Ma

Pliocene basalt flow with an underlying subvertical contact with 160-180 Ma Hunter Mountain batholith against country rock. Reconstruction of this marker suggests 8-10 km of dextral motion along the Hunter Mountain fault with <1 km of vertical motion. Burchfiel et al. [1987] argue that the limited change in elevation of this piercing point requires displacement on a <15º-dipping fault. However, Westaway [1999] dismisses the piercing point argument, suggesting that little vertical motion is expected along a dominantly strike-slip fault.

A related geophysical investigation focused on the northern part of Panamint Valley found that the thickness of basin sediments is <300 m, indicating minimal vertical motion, which the authors interpret is consistent with the presence of a LANF beneath Panamint Valley [*MIT Field Geophysics Course and Biehler*, 1987]. Those results are consistent with exploratory drilling in the northern Panamint Valley where basement rocks were encountered at a depth of ~110 m in drill hole 2 (DH-2) (Fig. 2) [*Smith and Pratt*, 1957]. Low frictional values of fault gouge sampled from the Panamint LANF range from 0.28 to 0.38 and highlight the role that high clay content may play in facilitating slip on a shallowly dipping fault [*Haines et al.*, 2014; *Numelin et al.*, 2007]. This result is similar to the inference that the Panamint LANF is no more than one third as strong as unbroken rock, based on calculations relating the shallow dip of the LANF (~7.5º) and motion on a slip vector toward 300-310º [*Wesnousky and Jones*, 1994]. Furthermore, Plio-Pleistocene fan gravels are documented to occur stratigraphically above mylonite and the range front LANF in exposures between Happy and Redland Canyons, as well as south of Wildrose graben [*Andrew and Walker*, 2009; *Cichanski*, 2000; *Kirby*, 2016]. Importantly, the contact between the fan gravels and bedrock is planar and shows evidence for brittle deformation. These relationships suggest that this is a fault contact, as opposed to being depositional in nature. Fan deposits that overly the LANF have not been directly dated; however,

burial dating focused on the nearby on the 180-m-thick Pleasant Canyon fan sequence (Fig. 2b) indicate a basal fan deposit age of ~1.55 Ma and fan abandonment at 0.36–0.52 Ma [*Mason and Romans*, 2018]. In summary, these observations point to brittle Quaternary motion along the Panamint LANF.

In contrast, Cichanski [2000] conducted detailed mapping focused on the western flank of the Panamint Range for ~15 km between Happy and Redlands Canyons. That study explores the geometric relationship of LANFs with higher-angle structures near the range front (Fig. 1). Based on a limited number of exposures of secondary structures (i.e., not the primary LANF), Cichanski [2000] concludes that the LANF is cut by higher-angle structures. A limitation of that study is that it presents limited observations of the first-order geometric relationships between the HAFs and LANFs in the region.

3. Methods

3.1. Geologic mapping

We used traditional structural and neotectonic mapping methods to document LANF and HAF features in the study area. Base maps included airborne lidar, 10-m resolution National Elevation Dataset, National Agriculture Imagery Program imagery, and WorldView imagery (see Acknowledgements). Geologic mapping at the Wildrose graben (Fig. 3) was compiled from Jayko [2009], U.S. Geological Survey (USGS) Quaternary fault database [*Machette et al.*, 2004], and our field-based mapping. We extracted topographic profiles at the sites using National Elevation Dataset 10 m resolution data (Fig. 4). Mapping at the playa site (Fig. 5) was compiled from Kirby [2016], Cichanski [2000], the USGS Quaternary fault database [*Machette et al.*, 2004], and our own mapping. Photographs document key map relationships at both sites (Fig. 6).

We distinguished and grouped alluvial fan deposits by following prior mapping and using differences in relative elevation, the degree of incision, and development of desert varnish and desert pavement, into very old (Qvoa, early Pleistocene), old (Qoa, middle to early Pleistocene), intermediate (Qia, late to middle Pleistocene), and young (Qya, Holocene and late Pleistocene) alluvial fan deposits. The playa site is situated ~6 km south of Pleasant Canyon, where the Qvoa and Qoa deposits correspond to the Pleasant Canyon fan sequence dated by Mason and Romans [2018], which ranges in age from 1.55 to 0.36 Ma.

3.2. Seismic reflection imaging methods

We acquired two high-resolution P-wave seismic reflection profiles using a minivib I trailer-mounted vibrator source. The northern profile (Profile 1) crosses the 2-km-wide Wildrose graben and the southern profile (Profile 2) extends onto the Panamint Valley playa, ~7.5 km S of Ballarat, CA (Figs. 3 and 5). The Wildrose graben survey was located within the boundary of Death Valley National Park and the playa survey was located on land administered by the Bureau of Land Management. In both cases, permit restrictions limited our access to preexisting roads. For the Wildrose graben survey in particular, this limitation resulted in a survey geometry that is oblique to the orientation of the graben axis.

The minivib swept from 20 to 180 Hz over 12 seconds for a 2 second record length. We used a single 8 Hz vertical component geophone per receiver station and a 5 m source and receiver spacing throughout acquisition of both profiles. We recorded 240 and 216 channels per field record on Profile 1 and Profile 2, respectively. Profile 1 was acquired with an asymmetric split spread (Fig. 3), while Profile 2 was acquired by a walkthrough approach. Profile 1 was ~4.68 km in total length. Profile 2 was approximately 1.08 km long; however, due to challenging

terrain and restricted access across the playa, the minivib source was limited to 85 stations spanning ~0.43 km of the total receiver array (Fig. 5). Although both profiles were in relatively remote areas with minimal cultural noise, the field records were impacted by noise due to air traffic and wind (Fig. 7). While noise is evident on these representative field records, particularly at greater source-receiver offsets, there are also clear reflections observed for both seismic profiles.

We applied conventional seismic data processing techniques [see *Yilmaz*, 2001], which included datum statics, amplitude correction, bandpass filter, dip filter to mitigate coherent noise, adaptive spiking deconvolution, and multiple iterations of velocity analysis and residual statics. Our results were converted to depth after post-stack, finite-difference time migration using a smoothed stacking velocity function optimized for each profile. We present results in the form of two-dimensional (2-D) profiles for both surveys. The length of these subsurface image sections for the Wildrose graben and playa surveys are 4.57 km and 0.79 km, respectively. Our results discussed below are presented in this 2-D profile subsurface reference frame (see blue lines in Figures 3 and 5). Raw correlated shot records and source/receiver location information are presented in a companion online repository [*Gold et al.*, 2020].

4. Results

4.1. Wildrose graben, Profile 1

Wildrose graben is defined by a north-south trending set of faults that offset Quaternary alluvial fans (Fig. 3 and 6a). Mappable geologic units in this study area include a package of Proterozoic metasedimentary rocks that form the Panamint Range to the east, a package of Mio-Pliocene clastic deposits to the north and alluvial fan deposits to the west (Fig. 3). The LANF is

exposed at the range front, where it places heavily weathered and incised alluvial fan deposits (Qvoa, early Pleistocene to Pliocene) in fault contact over the metasedimentary units (Fig. 6b). The Qvoa package is limited to the mouth of Wildrose Canyon near the range front. A sequence of younger Quaternary alluvial fan deposits span the area west of the Panamint range front, which include old (Qoa, middle to early Pleistocene), intermediate (Qia, late to middle Pleistocene), and young (Qya, Holocene and late Pleistocene) alluvial fan deposits. The Wildrose graben is so named based on the presence of two principal steeply dipping faults, HAF2 and HAF3, which form a 1–2 km wide graben, principally in the Qoa fan deposits (Figs. 3 and 6a). In addition, there are secondary faults throughout the graben. We documented evidence for distributed faulting that was recorded as sharp scarps in the axis of the graben on the Qya surface, in the southern portion of the map area (Figs. 3b and 6c).

Our seismic-reflection survey (Profile 1) trends obliquely to the orientation of the Wildrose graben and intersects three primary HAFs observed at the surface (Figs. 3 and 6-7). From NE to SW, they include HAF1, which dips ~65º and cuts Qvoa observed in exposures at the margins of Wildrose Canyon (kilometer 4.2); HAF2, a synthetic fault that defines the eastern margin of the Wildrose graben (kilometer ~3); and HAF3, an antithetic fault that defines the western margin of the Wildrose graben (kilometer 0.8). Additionally, ~1-km east of the NE terminus of Profile 1, the LANF is exposed at the range front and dips 15-20º to the WNW (Figs. 3 and 6b). Based on this orientation, we estimate that the LANF projects into the NE end of the reflection survey at an elevation of ~870-820 m (asl) with an apparent dip of 6-9º to the west (grey dashed lines in NE portion of Fig. 8c).

In the reflection data, we identify two primary domains (Fig. 8). Reflections in the upper domain are locally discontinuous, with significant noise, and extend from the surface to depths of

~80–200 m. The lower domain is characterized by more laterally continuous lower-frequency and layered reflections. We interpret the upper domain to correspond to alluvial fan deposits and the lower domain to correspond to foliated metamorphic rocks. The two domains are separated by the strongest impedance contrast observed in the survey. This reflection dips gently to the SW, with an average apparent dip of ~3º (6º with 2x vertical exaggeration, as depicted in Fig. 8). At the NE portion of the reflection profile, the elevation of this prominent reflection is ~825 m (asl). The elevation and attitude of the strong impedance contrast are in close agreement with the expected orientation and location of the LANF at the NE end of the survey (Fig. 8c). This finding leads us to interpret that the impedance contrast represents the LANF separating unconsolidated alluvial fan material from foliated metamorphic rocks in the footwall.

We do not image HAFs directly, but we infer them from apparently offset or disrupted reflections and zones of inclined and truncated reflections. From east to west, these include synthetic faults, HAF1 (kilometer 4.3) and HAF2 (kilometer 3.3 to 3.5), and antithetic fault, HAF3 (kilometer 0.9 to 1.2), as well as secondary faults within the graben (kilometer 1.8 to 2.6) and also west of F3 (kilometer 0.3 to 0.7) (Fig. 8).

The three primary HAFs we observe in the reflection image appear to cut the LANF surface (Fig. 8). Specifically, HAF1 and HAF2 fault the LANF down to the west 10 m and 80 m, respectively. Antithetic fault HAF3 displaces the LANF ~40 m down to the east. These relationships suggest ~50 m of net down to the west faulting of the LANF. However, the oblique orientation of our reflection line, relative to the strike of the HAFs, challenges our ability to robustly calculate net displacement. We correct for apparent dip associated with the oblique orientation of the seismic reflection profile relative the trend of the HAFs observed in map view, which yields the following dips for the HAFs: HAF1, 63ºW; HAF2, 65ºW; and HAF3, 43ºE. In

the discussion, below, we use this dip information to estimate net vertical and horizontal motion on these faults.

4.2. Playa, Profile 2

The southern study area that extends onto the Panamint Valley playa (Fig. 5 and 6) is characterized by three primary geologic units, which from east to west include mylonitic leucogranite that composes the Panamint Range, a package of alluvial fans, and playa sediments. The LANF is exposed at the range front, where it places the oldest alluvial fan deposits (Qvoa, early Pleistocene) in fault contact over the Proterozoic mylonitic leucogranite (Fig. 6b). The Qvoa package is interpreted to be correlative with ~1.55 Ma basal deposits of the Pleasant Canyon fan complex, ~6 km to the north [*Mason and Romans*, 2018]. The Qvoa package is covered by an incised alluvial fan surface (Qoa) that is ~25 m above the modern fan surface (Fig. S1). The Qoa deposit is interpreted to be correlative with the uppermost 0.36–0.52 Ma Pleasant Canyon fan complex [*Mason and Romans*, 2018]. Intermediate fan deposits (Qia) are preserved west of the range front and are ~10 m above the modern surface (Fig. S1). The young fan deposits in the map area (Qya) are prevalent west of the range front and are interpreted to interfinger with playa deposits that are within the basin.

Faulting in this area from east to west includes the LANF at the range front and a series of HAFs that cut the alluvial fan deposits. The range-bounding fault, HAF1, is defined by a linear, ~40 m wide graben. Several of the more western fault strands exhibit geomorphic evidence for right-lateral faulting, including laterally deflected gullies on the alluvial fan surface, consistent with mapping in adjacent drainages [*Sethanant*, 2019].

The southern survey (Profile 2) extends from the Panamint range front west onto the Panamint Valley playa (Fig. 5). The 0.79-km long profile generated from this survey trends orthogonal to the range front and intersects three HAFs. At the surface, these include a west dipping fault, HAF2, an antithetic east-dipping fault, HAF3, and a west-dipping fault, HAF4 (Fig. 9). A lack of passable terrain prevented us from extending the survey east to the prominent graben-forming fault (HAF1) system at the range front and the west-dipping LANF. The LANF separates mylonitic leucogranite in the footwall from alluvial fan deposits in the hanging wall. The LANF dips 25-30º to the WSW (Fig. 6d). Based on this orientation and before accounting for any displacement across HAF1, we estimate the LANF would project into the east end of the survey at an elevation of ~330 m (asl).

We identify three primary domains in the reflection image of Profile 2 (Fig. 9). The upper domain is chaotic, similar to the upper domain of Profile 1, and extends from the surface to depths of ~200 m. We interpret these poorly defined reflections to correspond to alluvium, which is characterized by poor internal sorting and significant along-strike heterogeneity. The second domain at intermediate depths (0-400 m below the surface) is characterized by high frequency, well-layered reflections. We interpret these reflections to correspond to subsurface lacustrine deposits, which are consistent with their coherence and lateral continuity. This interpretation is logical based on the proximity to the active Panamint Valley playa and the pluvial lake history of the basin [*Jayko et al.*, 2008; *R Smith*, 1976] and is consistent with core material recovered from drill holes DH-1 and DH-3 in the basin (Fig. 2b) [*Smith and Pratt*, 1957]. The third and deepest (>200 m below the surface) domain consists of low-frequency reflections with moderate lateral continuity. We interpret this domain to correspond to the mylonitic leucogranite.

The lacustrine and fanglomerate material in the upper two domains of Profile 2 is separated from the crystalline rocks of domain 3 by a strong impedance contrast (Fig. 9). In the western portion of the profile (kilometers 0 to 0.6), this impedance contrast dips gently (~5-15º) to the east. In the eastern portion of the profile, the impedance contrast dips gently (10-30º) to the west. We interpret this impedance contrast as corresponding with the LANF observed at the range front at the surface. However, the mapped surface trace of the LANF at the range front projects into the eastern end of the reflection survey at an elevation of ~330 m (asl), which does not match the observed depth (elevation of ~70 m asl) of the strong impedance contrast at this location (Fig. 9). We propose that these disparate depths can be reconciled by significant (~260 m vertical separation) dip-slip motion on HAF1 observed at the surface just beyond the end of our reflection survey (Figs. 5 and 9). This interpretation is consistent with the observation north of Profile 2 that HAF1 displaces and buries alluvial fan unit Qvoa and juxtaposes fan packages Qvoa and Qia (Fig. 5).

The east-dipping panel of the LANF imaged from kilometer 0 to 0.6 cannot easily connect with the surface projection of the LANF (Fig. 9). Furthermore, the package of lacustrine deposits and the overlying contact separating the lacustrine and alluvium domains both dip gently to the east. The simplest explanation for these geometric relationships is that the Quaternary sediment package, LANF, and bedrock west of kilometer 0.7 have experienced clockwise rotation due to slip along high-angle structure HAF2 that includes either listric geometry or significant lateral motion (Fig. 9).

In addition, we observe a number of steeply dipping faults in the reflection image (Fig. 9). In general, these faults correspond to fault scarps visible at the surface. The westernmost fault, HAF4, is cryptic in the reflection image, though it appears to disrupt the LANF and

overlying lacustrine reflectors. Antithetic fault HAF3, dips steeply to the east and offsets the lacustrine reflectors and the LANF. Synthetic fault, HAF2, is multi-stranded and cuts the LANF and overlying lacustrine and alluvial reflectors. The LANF is interpreted to be down-dropped ~80 m (down to the west) across this zone of faulting. We interpret variable thickness in the stratigraphic packages across the principal faults to be the result of strike-slip motion, which is consistent with the steep orientation of faults associated with HAF2 in the reflection image, the linear faults in map view (e.g., HAF1), and evidence for strike slip motion recorded on the alluvial fan surfaces (e.g., HAF3).

These interpretations are consistent with drilling in the central part of Panamint Valley (Fig. 2b), where lacustrine deposits including clay and evaporites were encountered down to depths ~300-m below the surface [*Smith and Pratt*, 1957]. Neither DH-1 (152 m deep) nor DH-3 (303 m deep) encountered bedrock or the LANF. DH-3 is located ~2.3 km west of the range front, approximately 2.5 km south of Profile 2 (Fig. 2b). Assuming a continuous west dip of 25º, accounting for topography, and ignoring any potential vertical displacement across high-angle faults, we would expect the LANF at a depth >1000 m below the surface. That prediction is consistent with the interpretations above.

5. Discussion

5.1. Low-angle normal fault cut by high-angle faults

A first-order result from both seismic reflection surveys is that the strong impedance contrast we interpret as the LANF appears to be faulted and displaced by the higher-angle faults in the upper 200-300 m. This result suggests that at least at shallow (<300 m) depths, the LANF

imaged is no longer a seismically capable source. This result has important implications for tectonic evolution of the region, which we explore below.

In Profiles 1 and 2, we observe subhorizontal to moderately dipping, strong impedance contrasts at shallow depths that project toward LANFs mapped along the Panamint range front (Figs. 8 and 9). We interpret these impedance contrasts as LANFs, given clear surface observations of low-angle faulting and juxtaposed alluvium and bedrock along the Panamint range front. The imaged LANFs are not continuous across the survey profiles (Figs. 8 and 9) and the imaged LANF in Profile 2 does not project directly to the mapped LANF surface trace. Instead, LANFs in both Profiles 1 and 2 appear faulted, vertically displaced, and locally rotated. This geometry is especially pronounced along Profile 2, where the LANF appears to be down dropped and back-rotated along a series of high-angle faults. We observe greater apparent vertical separation in Profile 2 (260 m, Fig. 9) compared to Profile 1 (50 m, Fig. 10a). This difference in apparent vertical separation is unsurprising given the significant distance between Profiles 1 and 2 (~28 km), over which we would expect changes in net dip-slip motion, especially with a significant component of strike-slip faulting. The observation that the LANF appears vertically displaced in the seismic reflection images is consistent with map relationships that show the formerly continuous Emigrant detachment is cut by the high-angle Panamint Valley fault zone [*Andrew and Walker*, 2009]. In map view, the Panamint Valley fault zone is both more laterally continuous than the traces of the Emigrant and Panamint LANFs, and crosscuts the LANF such that the LANF is not observed for nearly 14 km between Ballarat and south of Wildrose graben (Fig 2).

The interpretation that the LANF is offset by HAFs and is now inactive, particularly for the seismic line collected across Wildrose graben, has a number of caveats and potential

limitations. First, the seismic reflection imaging is limited to the shallow (<500 m) subsurface within a few kilometers of the western margin of the Panamint range front. Therefore, the LANF is possible active either to the west or at greater depths than is resolvable with our reflection surveys. Second, seismic reflection imaging is most sensitive to resolving significant impedance contrasts. In the Panamint Valley region, the strongest impedance contrasts in our surveys are between Quaternary alluvial fan and/or lacustrine sediments and bedrock, which at the surface, corresponds to the LANF contact. An active LANF possibly exists deeper within the bedrock, which is not resolvable with the reflection imaging acquisition parameters employed in this study. In this case, we might envision a scenario where the LANF visible in outcrop at the range front has been abandoned and that a deeper structure is active today (Fig. 10); however, mapped evidence of a deeper LANF that crops out east of the currently mapped surface trace of the LANF is lacking. Third, the interpretation that the LANF is offset by HAFs is difficult to reconcile with the lack of significant net vertical displacement across the Wildrose graben. Specifically, the old alluvial fan surface (Qoa) that is cut by the synthetic and antithetic HAFs records <10 m of apparent net vertical displacement (Fig. 4). A limitation with this treatment is that we lack constraints on the magnitude of younger alluvial fill and/or downcutting and spatial variations within the graben, which could lead to either larger or smaller true net vertical displacement estimates. Similarly, a lack of geochronologic constraints correlating the Qoa fan surfaces across the graben could result in miscorrelation of these surfaces, in the event they are different in age. However, if the correlations are correct as mapped, the lack of significant net vertical displacement across a wide graben with HAFs that independently offset the LANF 10 – 80 m vertically could be consistent with a deeper low-angle normal fault [*Axen et al.*, 1999] (Fig.

10b). Alternatively, the lack of significant vertical displacement on the high-angle structures could be the result of dominant strike-slip faulting on the HAFs (Fig. 10c).

To further explore the possibility of a deeper decollement underlying the Wildrose graben, we calculate net heave and throw, using the true dips of the HAFs and the magnitude of vertical separation of the LANF in the seismic reflection image. This set of calculations resolves a net throw of ~50 m (down to the west) and a net heave of ~90 m (Fig. 10a). These relationships imply that this displacement could be resolved on a low-angle normal fault dipping ~31º to the west (Fig. 10). As previously mentioned, this type of calculation could yield erroneous results if there is a significant component of lateral motion on the HAFs, which is a distinct possibility given the tectonic setting and observed strike-slip faulting along the Hunter Mountain fault to the north [*Oswald and Wesnousky*, 2002] and Panamint Valley fault zone to the south [*Zhang et al.*, 1990]. To summarize, the reflection data permit the presence of a deeper seismogenic LANF beneath Wildrose graben; however, the LANF imaged across Wildrose graben is definitively cut by high-angle structures.

The argument for a deeper LANF is not viable when considering Profile 2, which extends onto the playa (Fig. 10). Along Profile 2, we infer >260 m of net vertical displacement of the LANF, as well as significant back-rotation of the LANF surface in the western portion of the profile. Vertical displacement of this magnitude over a limited horizontal distance (~200-300 m), along with significant rotation, can best be explained via displacement across a steeply inclined fault. Although local back-rotation of the LANF could be controlled by a decrease in dip of the HAFs below the subsurface extent of profile 2 (similar to the geometry suggested in Fig. 10b), no evidence supports low-angle faulting within the crystalline bedrock. In summary, the

reflection results from both survey lines are most easily explained by recent dominant high-angle faulting, which have crosscut the LANF.

5.2. Tectonic evolution of Panamint Valley region

A significant number of observations suggest the LANF responsible for exhumation of the Panamint Range has been active from the Miocene to the middle to late Pleistocene. Results from this study are consistent with previous interpretations that suggest a dramatic shift in the style of tectonic deformation in this region in the past few million years [*Andrew and Walker*, 2009; *Burchfiel et al.*, 1987; *Gan et al.*, 2003; *Unruh et al.*, 2009]. An explanation for the seismic data reported here is that displacement on the LANF shut down in Plio-Pleistocene time and the region has most recently been dominated by dextral shear and dip-slip motion on steeply dipping normal faults. This transition could be later than the onset of dextral shear in the region, estimated to have initiated ~5 Ma [*Gan et al.*, 2003]. The region underwent a significant change in the distribution of dextral shear after ca. 2.0-3.5 Ma [*Unruh et al.*, 2009]. Therefore, high-angle dextral oblique faulting possibly became the dominant style of deformation as part of reorganization of shear in the southern Walker Lane. Constraints on the age of the Pleasant Canyon fan complex, which was deposited <1.55 Ma [*Mason and Romans*, 2018] may place a maximum constraint on the timing of LANF abandonment and the onset of high-angle faulting associated with the Panamint Valley fault zone in Panamint Valley.

5.3. Implications for seismic hazard modeling

Results from this seismic reflection survey suggest that the LANF bounding the western margin of the Panamint Range is no longer active. As discussed above, there are caveats to this

interpretation, particularly the possibility that a deeper <30º dipping fault may exist at depths greater than the aperture of the reflection study. However, the simplest explanation of the data is that the LANF has been overprinted by steeply dipping faults in Panamint Valley, including the Panamint Valley fault zone, Ash Hills fault, and northerly Hunter Mountain fault. Although we might expect that the LANF is able to produce higher levels of ground shaking given a larger cross-sectional area through the seismogenic crust, numerical models suggest that LANFs can slip only in a slip-hardening regime [e.g., *Lecomte et al.*, 2012]. Therefore, the overprinting by HAFs may effectively increase seismic hazard in the region by allowing large ruptures on HAFs rather than creep or smaller ruptures associated with LANF slip.

For seismic hazard modeling purposes, our analysis favors a logic-tree approach [e.g., *Petersen et al.*, 2014] to encapsulate epistemic uncertainty regarding the dominant style of faulting in Panamint Valley. For example, a steeper fault could be given a higher weight (e.g., 0.8) and a low-angle geometry (<30º) a low weight (e.g., 0.2). This approach would honor the findings from this reflection survey, while also respecting lines of evidence that indicate the LANF played a critical role in the development of Panamint Valley: evidence for 8-10 km of dextral motion along the <15º-dipping Hunter Mountain fault [*Burchfiel et al.*, 1987]; basin sediment thickness <300 m, indicating limited dip slip along HAFs [*MIT Field Geophysics Course and Biehler*, 1987]; and <1.55 Ma [*Mason and Romans*, 2018] fan gravels in fault contact with the LANF at numerous localities along the western flank of the Panamint Range [*Andrew and Walker*, 2009; *Kirby*, 2016]. These lines of evidence suggest that as recently as <1.55 Ma, the LANF may have been the dominant style of faulting in the region. Therefore, it appears prudent to consider the seismogenic potential of these structures in seismic hazard modeling, despite a lack of current activity along the shallow portions of the Panamint LANF.

Conclusions

This seismic reflection dataset documents the geometric relationship between high-angle dextral-normal faults and a low-angle normal fault (LANF) along the western margin of the Panamint Range. Importantly, at two locations where the LANF is exposed at the range front, the LANF is cut and rotated by the steeply dipping faults. These relationships suggest that at least at shallow (<200-300 m) depths, the LANF is not a current active seismic source. Models of dominant high-angle faulting and a possible deeper LANF could be addressed in seismic hazard models using a logic-tree approach.

Acknowledgements

This manuscript benefitted from constructive reviews by Stephen Delong and two anonymous JGR reviewers, and Associate Editor Kristin Morell. Data acquisition supported by Alena Leeds, Jim Allen, Dolan Paris, David Worley, Israporn Sethanant, Wesley von Dassow and John Gosse. This work was conducted under permits issued by Death Valley National Park and the Bureau of Land Management Ridgecrest field office. Lidar data accessed from OpenTopography at https://doi.org/10.5069/G9G44N6Q. WorldView imagery accessed under NextView license (©DigitalGlobe 2020) at https://evwhs.digitalglobe.com/. National Agriculture Imagery Program imagery accessed from https://datagateway.nrcs.usda.gov/. Topography from the 10-m National Elevation Dataset accessed from https://viewer.nationalmap.gov/advanced-viewer/. Raw correlated shot records and source/receiver location information are available from Gold et al. [2020, https://doi.org/10.5066/P9YY18PF]. This work was supported by the U.S. Geological Survey Earthquake Hazards Program. Any use of trade, product, or firm names is for descriptive purposes only and does not imply endorsement by the U.S. Government.

Figures

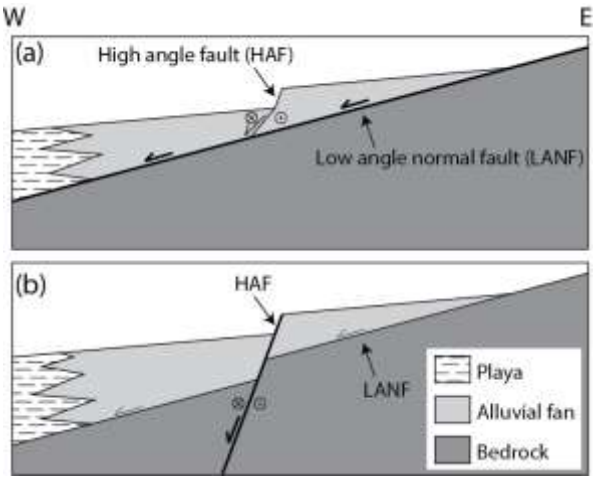

Figure 1. Cross section depicting idealized representation of two fault intersection scenarios [modified from *Cichanski*, 2000]. (a) The low-angle normal fault (LANF) is the most recently active structure. The high-angle (steeply dipping) fault (HAF) soles into the LANF. (b) The HAF is the active structure and cuts the shallowly dipping fault.

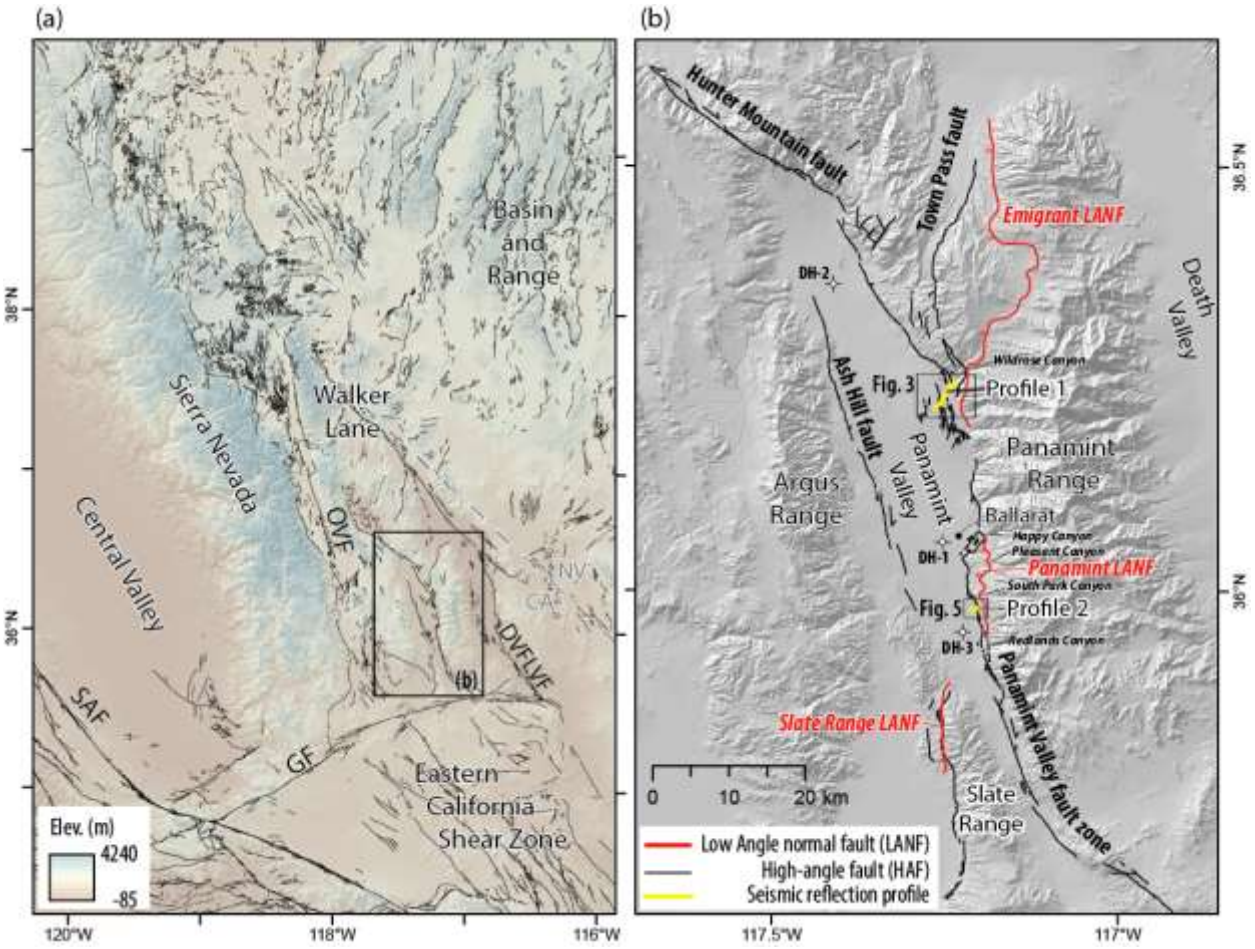

Figure 2. (a) Location of Panamint Valley in the context of the Walker Lane and Eastern California shear zone and Basin and Range, dominated by dextral shear and extension. Faults from USGS Quaternary fault database [*Machette et al.*, 2004]. SAF, San Andreas Fault; GF, Garlock fault; DVFLVF, Death Valley-Fish Lake Valley fault; OVF, Owens Valley fault. (b) Simplified map of low-angle normal faults (LANFs, red lines) and Quaternary dextral, normal, and dextral-oblique faults (black lines) in Panamint Valley, compiled from Jayko [2009], Kirby [2016], Cichanski [2000], the USGS Quaternary fault database [*Machette et al.*, 2004], and our own mapping. Yellow lines correspond to the seismic-reflection profiles presented in this study. Drill holes indicated by circle with cross in background [*Smith and Pratt*, 1957].

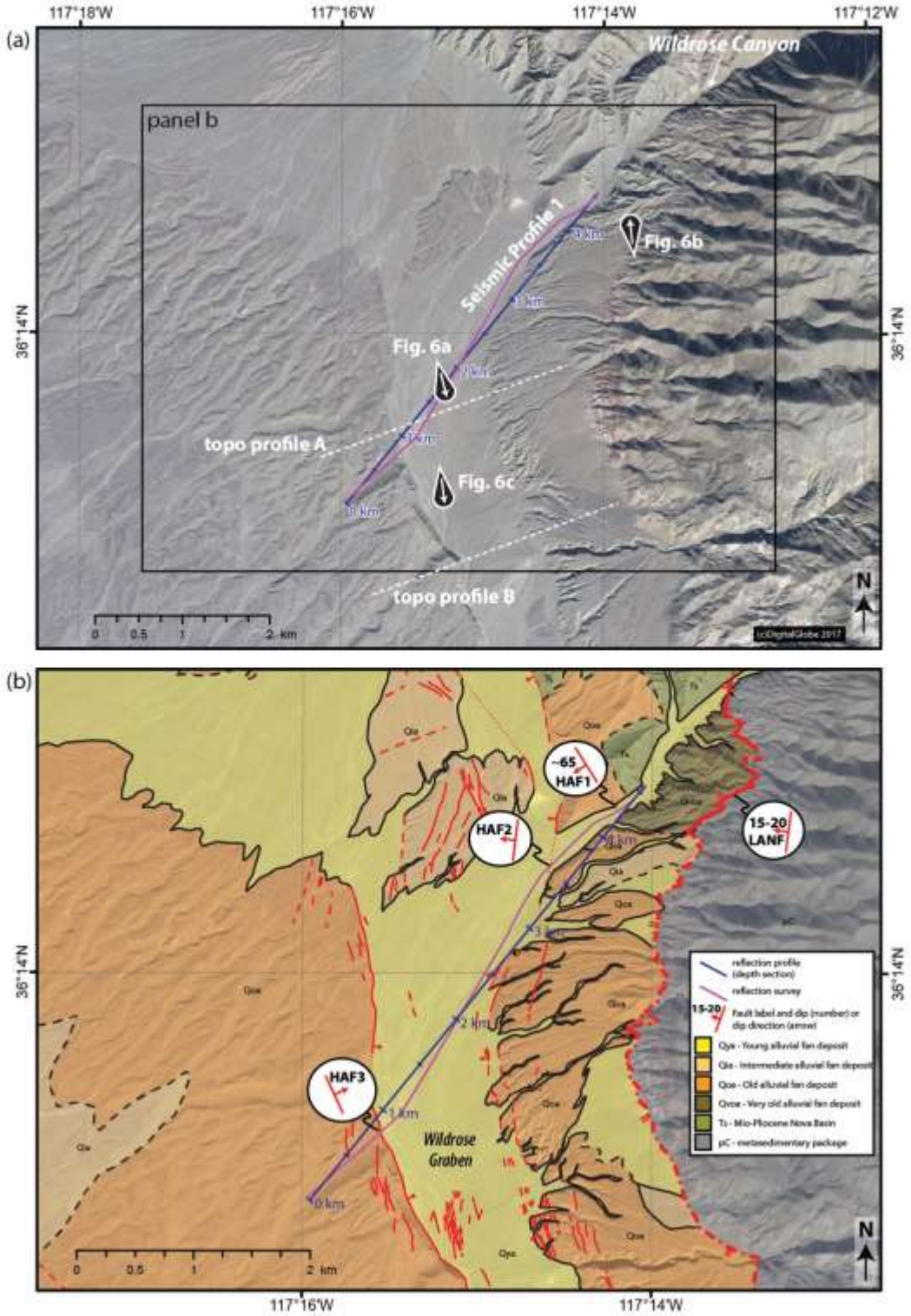

Figure 3. Wildrose graben site map. (a) Uninterpreted WorldView-2 satellite image (collection date: 14 November 2017, ©2017 Digital Globe, NextView License), with seismic reflection line (magenta). Blue line depicts 4.57-km-long profile onto which seismic reflection data are projected. Dashed white lines show topographic profiles presented in Figure 4. Look direction and location of field photographs (Fig. 6) indicated by black balloon shapes with inset arrows.

(b) Geologic mapping compiled from Jayko [2009], USGS Quaternary fault database [*Machette et al.*, 2004], and mapping from this study. Orientation of the low-angle normal fault (LANF, bold red line with double barb indicating dip to the west) and easternmost high-angle fault (HAF1) determined in the field. Orientations of HAF2 and HAF3 estimated from topography.

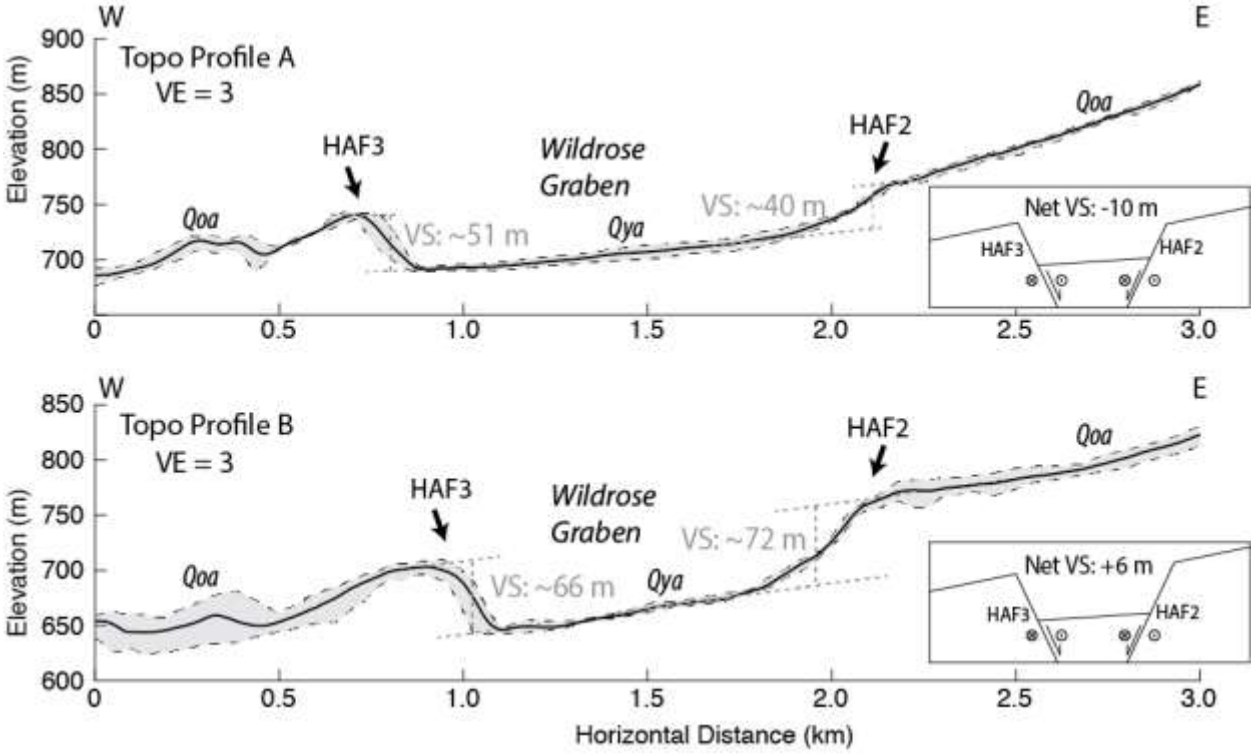

Figure 4. Topographic profiles across the Wildrose graben showing limited net vertical separation (VS) recorded by the old alluvial (Qoa) surface across HAF3 (antithetic fault) and HAF2 (synthetic fault). Inset figures depict net VS, calculated by differencing values measured across HAF3 and HAF2. Topography extracted from 10-m National Elevation Dataset with a swath width 100 m. Minimum and maximum (gray polygon with dashed outline) and mean (bold) topography indicated. Vertical exaggeration (VE) is 3x in both profiles. Profile locations indicated on Figure 3a.

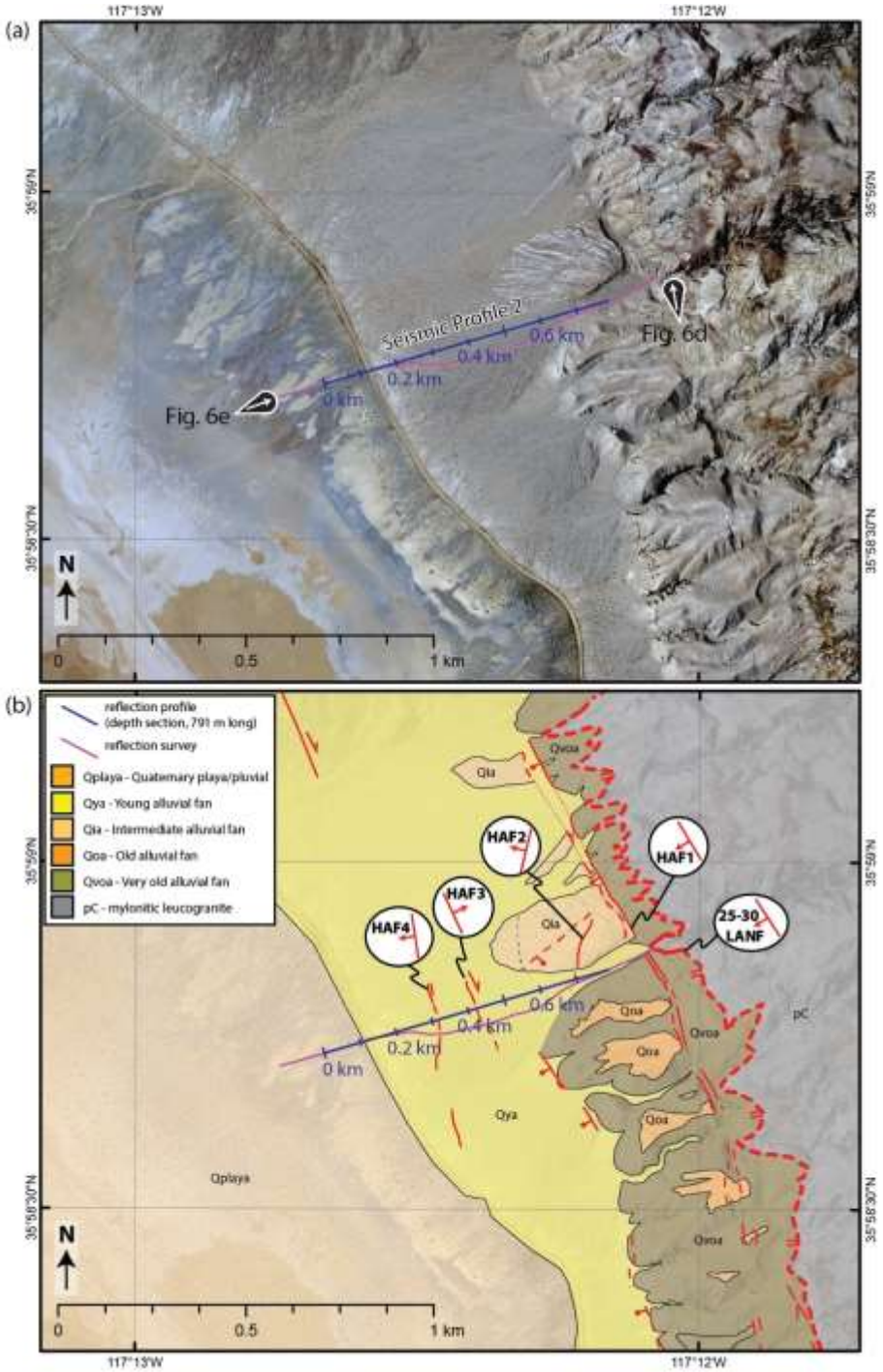

Figure 5. Playa site map. (a) Uninterpreted National Agriculture Imagery Program image, collected in 2018. Seismic reflection acquisition (magenta) and 0.79 km-long line seismic reflection projection line (blue) indicated. Look direction and location of field photographs (Fig. 6) indicated by black balloon shapes with inset arrows. (b) Geologic mapping, compiled from Kirby [2016], USGS Quaternary fault database [*Machette et al.*, 2004], and mapping from this study. Orientation of the low-angle normal fault (LANF) measured in the field. Orientations of dip direction and strike of high-angle normal faults (HAFs) estimated from topography using air photos and lidar.

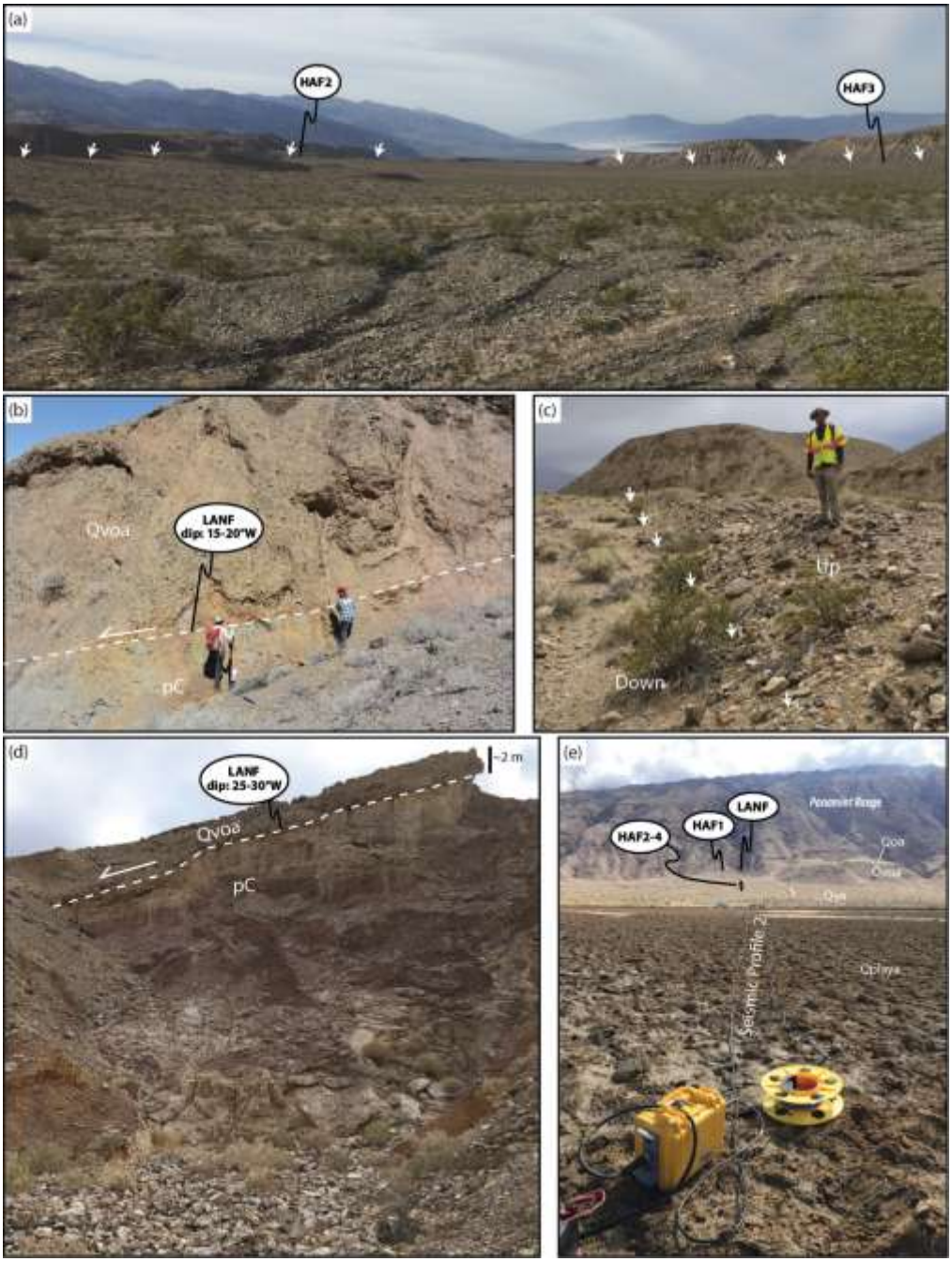

Figure 6. Field photographs. (a) Overview of Wildrose graben, looking south. High-angle faults, HAF2 (synthetic) and HAF3 (antithetic), define the margins of the graben and are indicated by white arrows. (b) Low-angle normal fault (LANF) characterized by fault gouge in exposure near Wildrose graben, separating Plio-Pleistocene alluvial fan material (Qvoa) from Proterozoic metasedimentary deposits (pC). (c) Youthful scarp in the axis of Wildrose graben indicated by white arrows. (d) LANF in exposure at east termination of Profile 2, dipping 25-30° to the west and separating Plio-Pleistocene alluvial fan material (Qvoa) from Proterozoic mylonitic leucogranite (pC). (e) Overview of Profile 2, looking east across the playa (Qplaya) and toward the Panamint Range. Location and view directions of photographs (a-c) indicated in Figure 3a and (d-e) in Figure 5a. Photographs taken April–May 2018 by R. Gold.

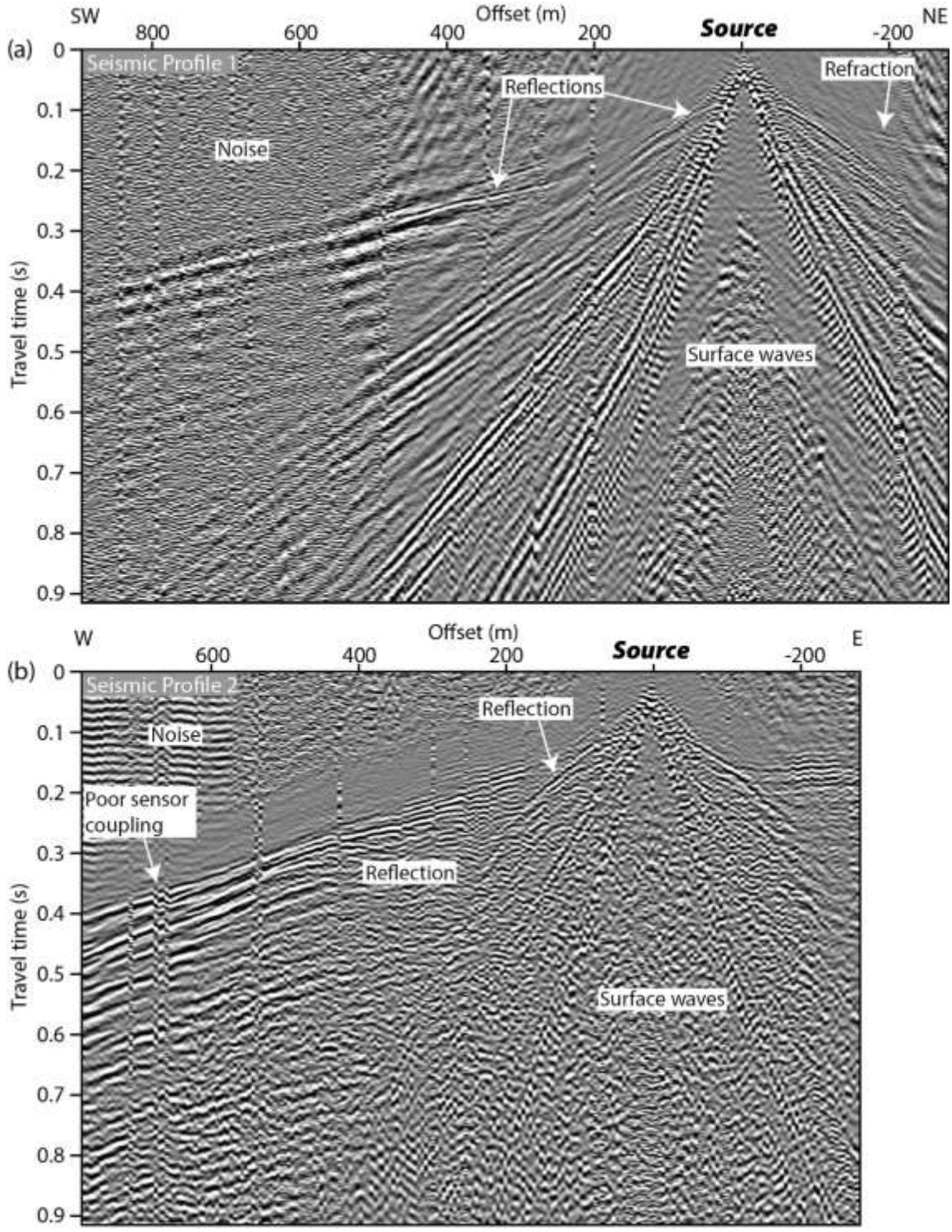

Figure 7. Representative field records from seismic-reflection survey. These field records have only bandpass filtering and gain correction applied. (a) Field record from Profile 1 shows several reflections, surface waves, and noise observed prior to the direct arrivals at far offsets contaminating the entire record. The minivib I source is located near HAF3, indicated in Figure 3. (b) Record from Profile 2 also shows several reflections, but a more poorly developed surface wavefield than on Profile 1.

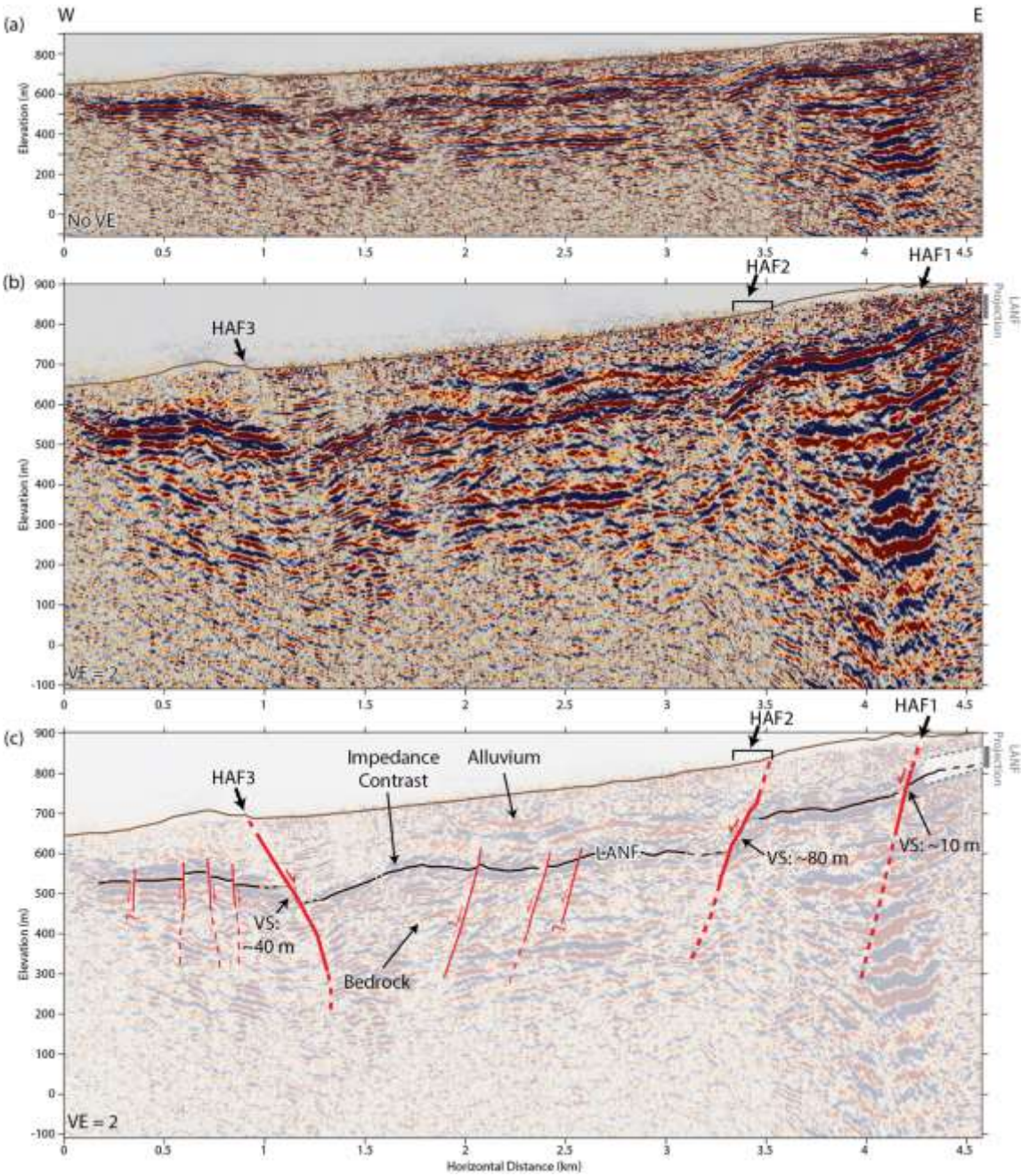

Figure 8. Seismic reflection Profile 1 across the Wildrose graben. (a) Uninterpreted reflection image with no vertical exaggeration. Topographic profile from 10-m National Elevation Dataset (brown line). (b) Same as (a), but with 2x vertical exaggeration (VE). Locations of high-angle faults (HAFs) at the surface indicated. Projection of the low-angle normal fault (LANF) into the northeastern portion of the profile indicated by gray bar and label. (c) Interpreted reflection image, indicating domains corresponding to alluvium and bedrock. HAFs represented by red lines and black line represents interpretation of LANF in seismic reflection image. Projection of LANF determined from surface measurements indicated by dashed gray lines, with attitude corrected to apparent dip. Importantly, the LANF is cut by the high-angle structures with vertical separation (VS) magnitudes reported. This relationship suggests that in this location, the LANF imaged is no longer active.

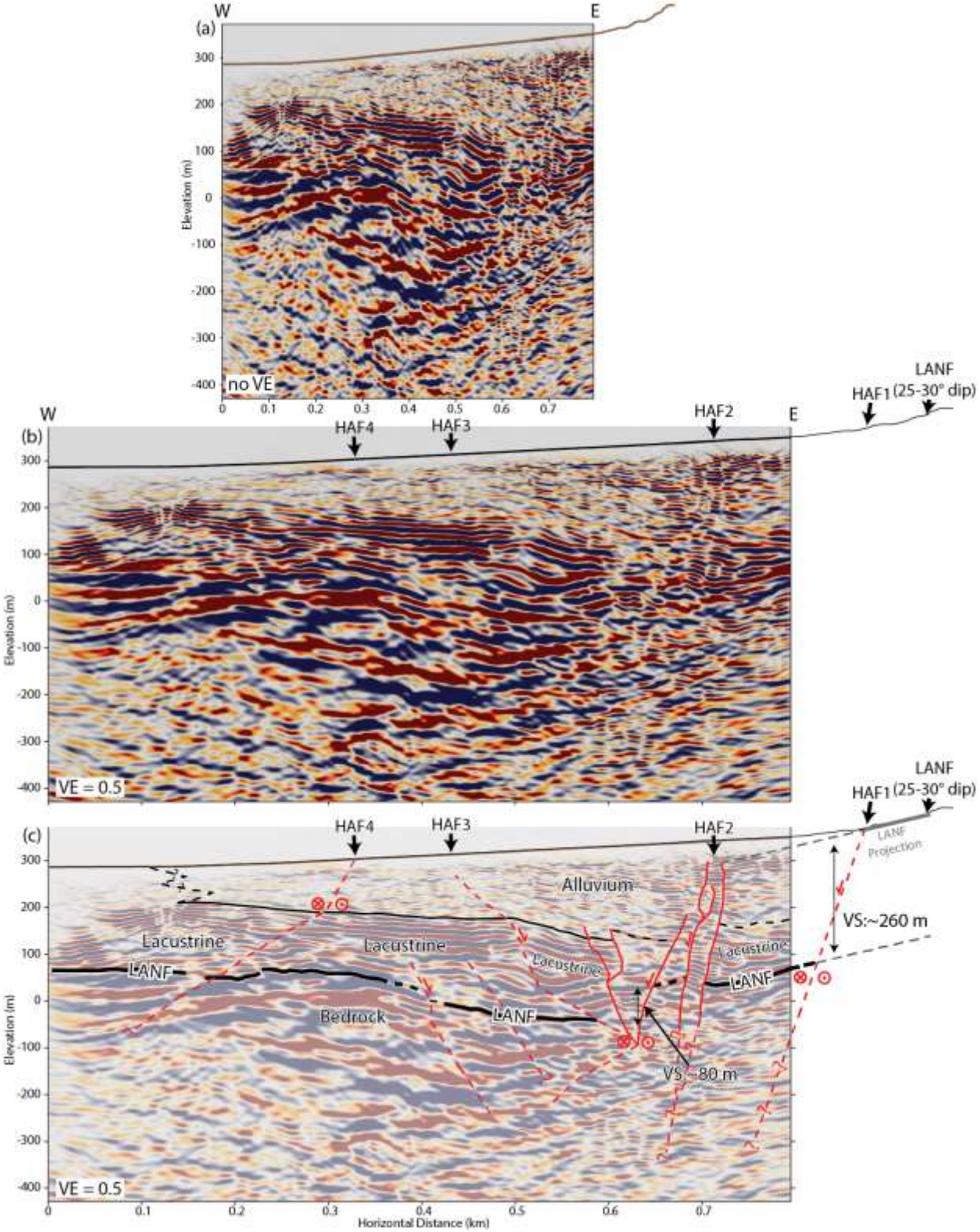

Figure 9. Seismic reflection Profile 2 onto the Panamint Valley playa. (a) Uninterpreted reflection image with no vertical exaggeration. Topographic profile from 10-m National Elevation Dataset (brown line). (b) Same as (a), but with half vertical exaggeration (horizontally stretched). Surface locations of high-angle faults (HAFs) and low-angle normal fault (LANF)

indicated. (c) Interpreted reflection image, indicating domains corresponding to alluvium, lacustrine deposits, and bedrock. Low-angle normal fault (LANF) and high-angle faults (HAFs) denoted. Projection of LANF from the surface into the reflection image indicated by dashed gray line. The LANF is vertically separated (VS) 74-88 m across HAF2. In the western portion of the reflection image, the LANF and overlying lacustrine reflectors are east-dipping, suggesting clockwise rotation. The intersection of the LANF with the range front graben high-angle fault is outside the aperture of the reflection image and also too shallow to be imaged. We propose a reconstruction, in which the LANF has been vertically separated (VS) ~260 m by the easternmost high-angle structure. This reconstruction suggests that in this location, the LANF imaged is no longer active in the near surface.

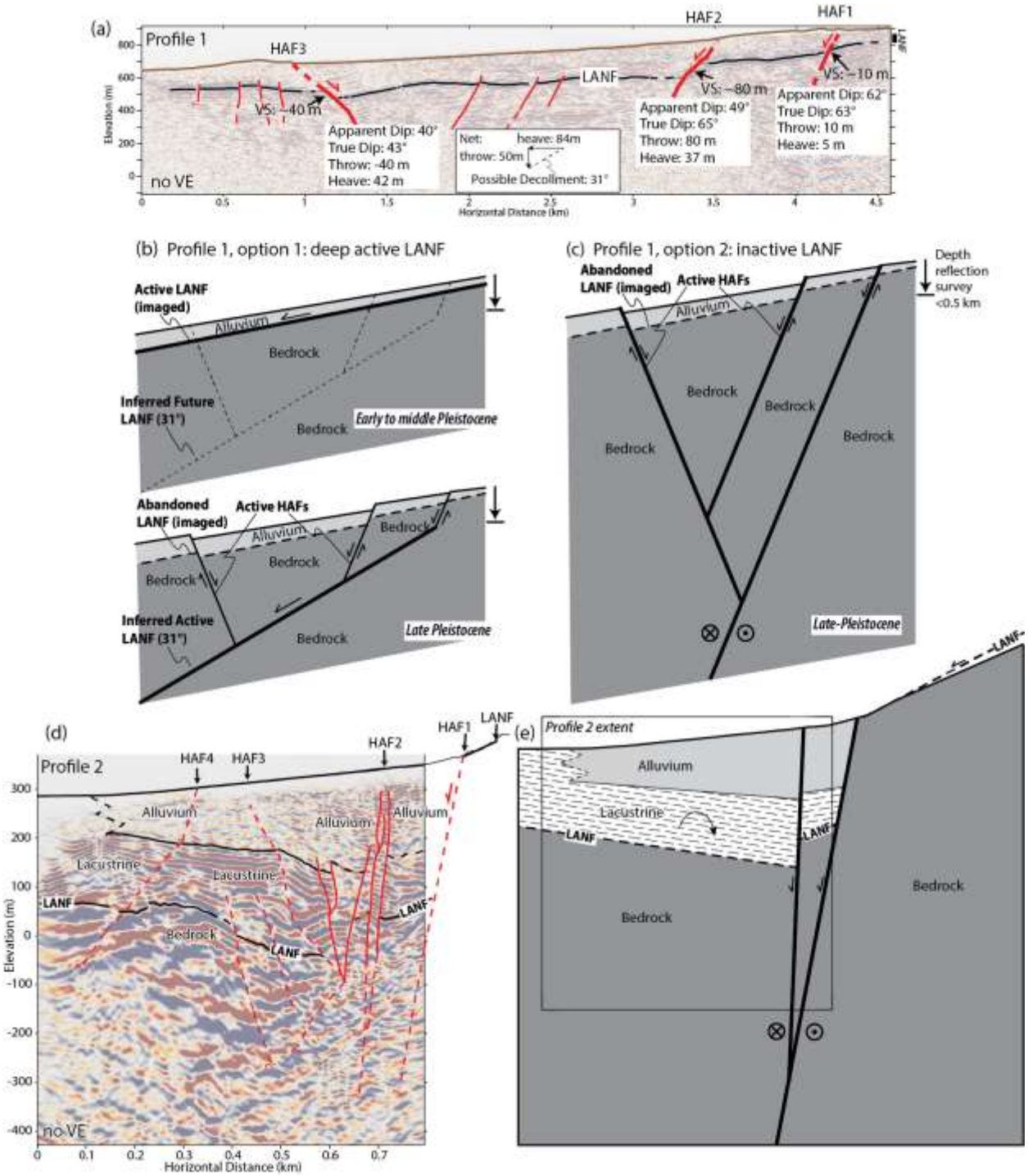

Figure 10. Seismic reflection Profiles 1 and 2 compared to schematic depictions of possible low-angle normal fault (LANF) and high-angle fault (HAF) cross-cutting relationships. (a) Subsurface calculations for Profile 1 across Wildrose graben (no vertical exaggeration) including vertical separation (VS) of the LANF, apparent dip and true dip of HAFs, and associated true heave across each HAF. Net throw across graben of LANF is ~50 m and net heave is ~84 m, implying that HAFs might sole into a ~31° dipping fault in the deeper subsurface (inset). (b) Schematic illustration of faults in the early to middle Pleistocene and latest Pleistocene, where the LANF imaged in this reflection study has been abandoned and deformation is now

accommodated by HAFs in the shallow subsurface (<0.5 km) and resolved onto a shallower master fault dipping ~31º. Importantly, this deeper 31º dipping fault could be difficult to detect in our reflection image given its depth and the possibility that it may place bedrock on bedrock, limiting sufficient impedance for seismic imaging purposes. (c) Alternative reconstruction across the Wildrose graben in which the HAF are dominant and the vertical separation measurements cannot be used given dextral-oblique motion across this portion of the Panamint Valley fault zone. (d-e) Profile 2, comparing the reflection image and a schematic illustration showing significant vertical displacement along HAF1 and rotation of the LANF and lacustrine deposits and normal-oblique motion along the Panamint Valley fault zone. Curved arrow in panel (e) indicates clockwise rotation of LANF and lacustrine deposits west of the primary zone of high-angle faulting.

References

Abbott, R. E., J. N. Louie, S. J. Caskey, and S. Pullammanappallil (2001), Geophysical confirmation of low-angle normal slip on the historically active Dixie Valley fault, Nevada, *Journal of Geophysical Research: Solid Earth*, 106(B3), 4169-4181, doi:10.1029/2000jb900385.

Albee, A. L. (1981), Geologic map of the Telescope Peak quadrangle, California, Report 1532.

Anderson, E. M. (1951), *The dynamics of faulting and dyke formation with applications to Britain*, Hafner Pub. Co.

Andrew, J. E., and J. D. Walker (2009), Reconstructing late Cenozoic deformation in central Panamint Valley, California: Evolution of slip partitioning in the Walker Lane, *Geosphere*, 5(3), 172-198, doi:10.1130/ges00178.1.

Axen, G. J. (2004), Mechanics of low-angle normal faults, in *Rheology and deformation of the lithosphere at continental margins*, edited by G. Karner, B. Taylor, N. Driscoll and D. Kohlstedt, pp. 46-91, Columbia University Press, doi:10.7312/karn12738-004.

Axen, G. J., J. M. Fletcher, E. Cowgill, M. Murphy, P. Kapp, I. MacMillan, E. Ramos-Velázquez, and J. Aranda-Gómez (1999), Range-front fault scarps of the Sierra El Mayor, Baja California: Formed above an active low-angle normal fault?, *Geology*, 27(3), 247-250.

Bennett, R. A., and S. Hreinsdóttir (2009), Active aseismic creep on the Alto Tiberina low-angle normal fault, Italy, *Geology*, 37(8), 683-686, doi:10.1130/g30194a.1.

Bruhn, R. L., P. R. Gibler, W. Houghton, and W. T. Parry (1992), Structure of the Salt Lake segment, Wasatch normal fault zone: Implications for rupture propagation during normal faulting, in *Assessment of regional earthquake hazards and risk along the Wasatch Front, Utah*, edited by P. L. Gori and W. W. Hays, pp. H1-H24, U.S. Geological Survey Professional Paper 1500.

Burchfiel, B., K. Hodges, and L. Royden (1987), Geology of Panamint Valley-Saline Valley pull-apart system, California: Palinspastic evidence for low-angle geometry of a Neogene range-bounding fault, *Journal of Geophysical Research: Solid Earth*, 92(B10), 10422-10426.

Byerlee, J. (1978), Friction of rocks, in *Rock friction and earthquake prediction*, pp. 615-626, Springer.

Caskey, S. J., S. G. Wesnousky, P. Zhang, and D. B. Slemmons (1996), Surface faulting of the 1954 Fairview Peak (MS 7.2) and Dixie Valley (MS 6.8) earthquakes, central Nevada, *Bulletin of the Seismological Society of America*, 86(3), 761-787.

Chiaraluce, L., C. Chiarabba, C. Collettini, D. Piccinini, and M. Cocco (2007), Architecture and mechanics of an active low-angle normal fault: Alto Tiberina fault, northern Apennines, Italy, *Journal of Geophysical Research: Solid Earth*, 112(B10), doi:10.1029/2007jb005015.

Cichanski, M. (2000), Low-angle, range-flank faults in the Panamint, Inyo, and Slate ranges, California: Implications for recent tectonics of the Death Valley region, GSA Bulletin, 112(6), 871-883, doi:10.1130/0016-7606(2000)112<871:Lrfitp>2.0.Co;2.

Collettini, C. (2011), The mechanical paradox of low-angle normal faults: Current understanding and open questions, *Tectonophysics*, 510(3-4), 253-268, doi:10.1016/j.tecto.2011.07.015.

Coney, P. J. (1987), The regional tectonic setting and possible causes of Cenozoic extension in the North American Cordillera, *Geological Society, London, Special Publications*, 28(1), 177-186, doi:10.1144/gsl.Sp.1987.028.01.13.

Coney, P. J., and T. A. Harms (1984), Cordilleran metamorphic core complexes: Cenozoic extensional relics of Mesozoic compression, *Geology*, 12(9), 550-554, doi:10.1130/0091-7613(1984)12<550:Cmccce>2.0.Co;2.

Crittenden, M. D., Jr., P. J. Coney, and G. H. Davis (1980), *Cordilleran Metamorphic Core Complexes*, Geological Society of America, doi:10.1130/mem153.

Densmore, A. L., and R. S. Anderson (1997), Tectonic geomorphology of the Ash Hill fault, Panamint Valley, California, *Basin Research*, 9(1), 53-63.

Gan, W., P. Zhang, Z.-K. Shen, W. H. Prescott, and J. L. Svarc (2003), Initiation of deformation of the Eastern California shear zone: Constraints from Garlock fault geometry and GPS observations, *Geophysical Research Letters*, 30(10), doi:10.1029/2003gl017090.

Gold, R. D., W. J. Stephenson, R. Briggs, C. DuRoss, E. Kirby, E. Woolery, J. Delano, J. K. Odum, and Coulsey R. (2020), Seismic reflection imaging of the low-angle Panamint normal fault system, eastern California, in *U.S. Geological Survey data release*, doi:10.5066/P9YY18PF.

Haines, S. H., C. Marone, and D. Saffer (2014), Frictional properties of low-angle normal fault gouges and implications for low-angle normal fault slip, *Earth and Planetary Science Letters*, 408, 57-65, doi:10.1016/j.epsl.2014.09.034.

Haines, S. H., and B. A. van der Pluijm (2012), Patterns of mineral transformations in clay gouge, with examples from low-angle normal fault rocks in the western USA, *Journal of Structural Geology*, 43, 2-32, doi:10.1016/j.jsg.2012.05.004.

Hodges, K., L. McKenna, J. Stock, J. Knapp, L. Page, K. Sternlof, D. Silverberg, G. Wüst, and J. D. Walker (1989), Evolution of extensional basins and Basin and Range topography west of Death Valley, California, *Tectonics*, 8(3), 453-467.

Hofffman, W. R. (2009), Late Pleistocene slip rates along the Panamint Valley fault zone, eastern California, 81 pp, Pennsylvania State University.

Hopper, R. H. (1947), Geologic section from the Sierra Nevada to Death Valley, California, *GSA Bulletin*, 58(5), 393-432, doi:10.1130/0016-7606(1947)58[393:Gsftsn]2.0.Co;2.

Hreinsdóttir, S., and R. A. Bennett (2009), Active aseismic creep on the Alto Tiberina low-angle normal fault, Italy, *Geology*, 37(8), 683-686, doi:10.1130/g30194a.1.

Jackson, J. A. (1987), Active normal faulting and crustal extension, *Geological Society, London, Special Publications*, 28(1), 3-17, doi:10.1144/gsl.Sp.1987.028.01.02.

Jayko, A. S. (2009), Surficial geologic map of the Darwin Hills 30′× 60′ quadrangle, Inyo County, California, *U.S. Geological Survey Scientific Investigations Map 3040*, scale 1:100,000.

Jayko, A. S., R. M. Forester, D. S. Kaufman, F. M. Phillips, J. C. Yount, J. McGeehin, and S. A. Mahan (2008), Late Pleistocene lakes and wetlands, Panamint Valley, Inyo County, California, in *Late Cenozoic Drainage History of the Southwestern Great Basin and Lower Colorado River Region: Geologic and Biotic Perspectives*, edited by M. C. Reheis, R. Hershler and D. M. Miller, pp. 151-184, Geological Society of America, doi:10.1130/2008.2439(07).

Kirby, E. (2016), *Friends of the Pleistocene, Pacific Cell 2016 Field Trip - Panamint Valley, CA*, 80 pp.

Labotka, T. C., A. L. Albee, M. A. Lanphere, and S. D. McDowell (1980), Stratigraphy, structure, and metamorphism in the central Panamint Mountains (Telescope Peak quadrangle), Death Valley Area, California, *GSA Bulletin*, 91(3_Part_II), 843-933, doi:10.1130/gsab-p2-91-843.

Lecomte, E., L. Le Pourhiet, and O. Lacombe (2012), Mechanical basis for slip along low-angle normal faults, Geophysical Research Letters, 39(3), doi:10.1029/2011gl050756.

Machette, M. N., K. M. Haller, and L. A. Wald (2004), Quaternary fault and fold database for the Nation, *U.S. Geological Survey Fact Sheet* 2004-3003.

Mason, C. C., and B. W. Romans (2018), Climate-driven unsteady denudation and sediment flux in a high-relief unglaciated catchment–fan using 26Al and 10Be: Panamint Valley, California, *Earth and Planetary Science Letters*, 492, 130-143, doi:10.1016/j.epsl.2018.03.056.

Maxson, J. H. (1950), Physiographic features of the Panamint Range, California, *GSA Bulletin*, 61(2), 99-114, doi:10.1130/0016-7606(1950)61[99:Pfotpr]2.0.Co;2.

McAuliffe, L. J., J. F. Dolan, E. Kirby, C. Rollins, B. Haravitch, S. Alm, and T. M. Rittenour (2013), Paleoseismology of the southern Panamint Valley fault: Implications for regional earthquake occurrence and seismic hazard in southern California, *Journal of Geophysical Research: Solid Earth*, 118, 5126–5146, doi:10.1002/jgrb.50359.

MIT Field Geophysics Course and S. Biehler (1987), A geophysical investigation of the Northern Panamint Valley, Inyo County, California: Evidence for possible low-angle normal faulting at shallow depth in the crust, *Journal of Geophysical Research: Solid Earth*, 92(B10), 10427-10441, doi:10.1029/JB092iB10p10427.

Mizera, M., T. A. Little, J. Biemiller, S. Ellis, S. Webber, and K. P. Norton (2019), Structural and Geomorphic Evidence for Rolling-Hinge Style Deformation of an Active Continental Low-Angle Normal Fault, SE Papua New Guinea, *Tectonics*, 38(5), 1556-1583, doi:10.1029/2018tc005167.

Morley, C. K. (2009), Geometry and evolution of low-angle normal faults (LANF) within a Cenozoic high-angle rift system, Thailand: Implications for sedimentology and the mechanisms of LANF development, Tectonics, 28(5), doi:10.1029/2007tc002202.

Numelin, T., C. Marone, and E. Kirby (2007), Frictional properties of natural fault gouge from a low-angle normal fault, Panamint Valley, California, *Tectonics*, 26(2), doi:10.1029/2005tc001916.

Oswald, J. A., and S. G. Wesnousky (2002), Neotectonics and Quaternary geology of the Hunter Mountain fault zone and Saline Valley region, southeastern California, *Geomorphology*, 42(3-4), 255-278, doi:10.1016/S0169-555X(01)00089-7.

Pang, G., et al. (2020), Seismic analysis of the 2020 Magna, Utah, earthquake sequence: Evidence for a listric Wasatch fault, *Geophysical Research Letters*, 47, doi:10.1029/2020GL089798.

Petersen, M. D., et al. (2014), Documentation for the 2014 update of the United States national seismic hazard maps, *U.S. Geological Survey Open File Report 2014-1091*, p. 243.

Proffett, J. M. (1977), Cenozoic geology of the Yerington district, Nevada, and implications for the nature and origin of Basin and Range faulting, *GSA Bulletin*, 88(2), 247-266, doi:10.1130/0016-7606(1977)88<247:Cgotyd>2.0.Co;2.

Sethanant, I. (2019), Late Holocene earthquake history recorded in alluvial fan sequences, Panamint Valley, eastern California, Oregon State University.

Sibson, R. H. (1994), An assessment of field evidence for 'Byerlee'friction, *Pure and Applied Geophysics*, 142(3-4), 645-662.

Smith, G., and W. Pratt (1957), Core logs from Owens, China, Searles, and Panamint basins, California, *U.S. Geological Survey Bulletin* (1045-A), 62.

Smith, R. (1976), Late-Quaternary pluvial and tectonic history of Panamint Valley, Inyo and San Bernardino Counties, California, California Institute of Technology.

Snyder, N. P., and K. V. Hodges (2000), Depositional and tectonic evolution of a supradetachment basin: 40Ar/39Ar geochronology of the Nova Formation, Panamint Range, California, *Basin Research*, 12(1), 19-30, doi:10.1046/j.1365-2117.2000.00108.x.

Stewart, J. H. (1988), Tectonics of the Walker Lane Belt, western Great Basin; Mesozoic and Cenozoic deformation in a zone of shear, in Rubey Volume, edited by W. G. Ernst, pp. 683-713, Prentice-Hall, Old Tappan, N.J.

Unruh, J., E. Hauksson, J. S. Oldow, and P. H. Cashman (2009), Seismotectonics of an evolving intracontinental plate boundary, southeastern California, in *Late Cenozoic Structure and Evolution of the Great Basin-Sierra Nevada Transition*, Geological Society of America, doi:10.1130/2009.2447(16).

Vadacca, L., E. Casarotti, L. Chiaraluce, and M. Cocco (2016), On the mechanical behaviour of a low-angle normal fault: the Alto Tiberina fault (Northern Apennines, Italy) system case study, *Solid Earth*, 7(6), 1537, doi:10.5194/se-7-1537-2016.

Webber, S., K. P. Norton, T. A. Little, L. M. Wallace, and S. Ellis (2018), How fast can low-angle normal faults slip? Insights from cosmogenic exposure dating of the active Mai'iu fault, Papua New Guinea, *Geology*, 46(3), 227-230, doi:10.1130/g39736.1.

Wernicke, B. (1995), Low-angle normal faults and seismicity: A review, *Journal of Geophysical Research: Solid Earth*, 100(B10), 20159-20174.

Wesnousky, S. G. (2005), Active faulting in the Walker Lane, *Tectonics*, 24(TC3009), 1-35, doi:10.1029/2004TC001645.

Wesnousky, S. G., and C. Jones (1994), Oblique slip, slip partitioning, spatial and temporal changes in the regional stress field, and the relative strength of active faults in the Basin and Range, western United States, *Geology*, 22(11), 1031-1034, doi:10.1130/0091-7613(1994)022<1031:Osspsa>2.3.Co;2.

Westaway, R. (1999), The mechanical feasibility of low-angle normal faulting, Tectonophysics, 308(4), 407-443, doi:10.1016/S0040-1951(99)00148-1.

Yilmaz, Ö. (2001), *Seismic data analysis: Processing, inversion, and interpretation of seismic data*, 2027 pp., Society of Exploration Geophysicists.

Zhang, P., M. Ellis, D. B. Slemmons, and F. Mao (1990), Right-lateral displacements and the Holocene slip rate associated with prehistoric earthquakes along the Southern Panamint Valley fault zone: Implications for southern Basin and Range tectonics and coastal California deformation, *Journal of Geophysical Research: Solid Earth*, 95(B4), 4857-4872, doi:10.1029/JB095iB04p04857.